NANO · MICRO small
www.small-journal.com

Interface Pattern Engineering in Core-Shell Upconverting Nanocrystals: Shedding Light on Critical Parameters and Consequences for the Photoluminescence Properties

Damien Hudry, Annick De Backer, Radian Popescu, Dmitry Busko, Ian A. Howard, Sara Bals, Yang Zhang, Adrian Pedrazo-Tardajos, Sandra Van Aert, Dagmar Gerthsen, Thomas Altantzis,* and Bryce S. Richards**

Advances in controlling energy migration pathways in core-shell lanthanide (Ln)-based hetero-nanocrystals (HNCs) have relied heavily on assumptions about how optically active centers are distributed within individual HNCs. In this article, it is demonstrated that different types of interface patterns can be formed depending on shell growth conditions. Such interface patterns are not only identified but also characterized with spatial resolution ranging from the nanometer- to the atomic-scale. In the most favorable cases, atomic-scale resolved maps of individual particles are obtained. It is also demonstrated that, for the same type of core-shell architecture, the interface pattern can be engineered with thicknesses of just 1 nm up to several tens of nanometers. Total alloying between the core and shell domains is also possible when using ultra-small particles as seeds. Finally, with different types of interface patterns (same architecture and chemical composition of the core and shell domains) it is possible to modify the output color (yellow, red, and green-yellow) or change (improvement or degradation) the absolute upconversion quantum yield. The results presented in this article introduce an important paradigm shift and pave the way toward the emergence of a new generation of core-shell Ln-based HNCs with better control over their atomic-scale organization.

1. Introduction

The synthesis of structurally and chemically well-defined core-shell hetero-nanocrystals (HNCs) is challenged by phenomena such as alloying (i.e., cation intermixing) and/or cation exchange reactions.[1] Furthermore, due to the difficulty in precisely characterizing the chemical distribution of elements in HNCs down to the atomic scale, such mixing processes can stay unnoticed. Underlying mechanisms are influenced by a delicate balance between intrinsic (e.g., lattice mismatch, chemical miscibility) and extrinsic (shell growth conditions) parameters, which ultimately govern the structural and chemical organization of core-shell HNCs.[2] Thus, in such highly crystalline but intrinsically non-periodic structures, precise information regarding the interface pattern is of major interest. Indeed, the latter, which describes the chemical and structural organization of

D. Hudry, D. Busko, I. A. Howard, B. S. Richards
Institute of Microstructure Technology
Karlsruhe Institute of Technology
Hermann-von-Helmholtz-Platz 1
76344 Eggenstein-Leopoldshafen, Germany
E-mail: damien.hudry@kit.edu; bryce.richards@kit.edu

The ORCID identification number(s) for the author(s) of this article can be found under https://doi.org/10.1002/smll.202104441.

DOI: 10.1002/smll.202104441

A. De Backer, S. Bals, Y. Zhang, A. Pedrazo-Tardajos, S. Van Aert, T. Altantzis
Electron Microscopy for Materials Science (EMAT)
University of Antwerp
Groenenborgerlaan 171, Antwerp 2020, Belgium
E-mail: thomas.altantzis@uantwerpen.be

A. De Backer, S. Bals, Y. Zhang, A. Pedrazo-Tardajos, S. Van Aert, T. Altantzis
NANOlab Center of Excellence
University of Antwerp
Groenenborgerlaan 171, Antwerp 2020, Belgium

R. Popescu, D. Gerthsen
Laboratory for Electron Microscopy
Karlsruhe Institute of Technology
Engesserstrasse 7, 76131 Karlsruhe, Germany

I. A. Howard, B. S. Richards
Light Technology Institute
Karlsruhe Institute of Technology
Engesserstrasse 13, 76131 Karlsruhe, Germany

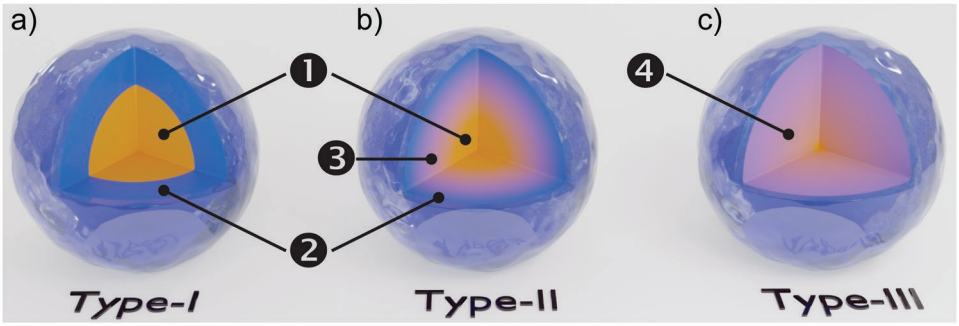

Figure 1. Schematic representation of the most common types of interface patterns that can be observed for core-shell hetero-nanocrystals (HNCs). a) Type-I or segregated model: abrupt interface with no intermixing between the core (orange color, ❶) and shell (blue color, ❷) domains. b) Type-II or interfacial alloying model: interfacial alloying with limited intermixing between the core and shell domains giving rise to an interphase domain (pinkish color, ❸). c) Type-III or global alloying model: extended intermixing that can lead to the total loss of the core and shell domains' integrity. In such an extreme case, the core and shell domains are replaced by an alloy (pinkish color, ❹) without or with chemical concentration gradients. Note that non-homogeneous alloying is possible for Type-II and Type-III interface patterns but was not represented for simplicity.

the 3D boundary/discontinuity region between core and shell sub-domains can vary from abrupt to diffuse (**Figure 1**). Consequently, the coupling between the sub-domains that constitute HNCs can be modified with potentially important consequences for macroscopic properties.[2c] For instance, interface pattern engineering is used in the fields of semiconductor[2b,3] and multi-metallic[4] HNCs as a guiding principle to control their optical or catalytic performance.

Over the past two decades, core-shell architectures have played a pivotal role in the development of lanthanide (Ln)-based ternary fluoride HNCs (with the general formula $NaLnF_4$),[5] which have risen as an important class of luminescent nanomaterials due to their upconverting capabilities.[6] Although compelling evidence of intermixing in Ln-based HNCs was published by several groups,[7] important parameters that influence the magnitude of intermixing are still unknown just like the consequences for the photoluminescence properties despite the early works reported in van Veggel's group.[8] This, together with the lack of details regarding the atomic scale organization of the 3D boundary/discontinuity region between the sub-domains, leads to a very limited understanding of the structure-property relationships in Ln-based HNCs although of critical interest, both on fundamental and applied levels.[9] Indeed, elementary photophysical processes that control the photoluminescence properties (for example emission spectrum, efficiency, and dynamics) of core-shell Ln-based HNCs, depend on energy exchange between optically active centers.[10] Since such energy exchanges are intimately linked to the available intra- and inter-domain energy migration pathways,[11] a realistic and accurate description of the spatial distribution (i.e., relative position and local concentration) of all optically active centers, and in particular within the 3D boundary/discontinuity region between the sub-domains, is of utmost importance. Because core-shell Ln-based HNCs share common features (i.e., fully inorganic nanostructures) with both semiconductor (e.g., very similar non-aqueous synthetic procedures in coordinating organic media) and multi-metallic (e.g., ability to form solid solutions over a wide range of chemical composition similar to metal alloys) HNCs, parameters known to modify the interface pattern of semiconductor and multi-metallic HNCs can have similar effects on Ln-based HNCs.

In this article, 15 years after the introduction of core-shell Ln-based HNCs,[12] the spatial distribution of chemical elements supposed to be confined in the core and shell sub-domains is revealed for the first time with atomic scale precision for entire individual particles (Part I). This article also introduces critical parameters such as the size of the starting core particles (acting as seeds for shell growth) along with the relative shell thickness, the nature of shell precursors, or post-synthesis annealing treatment as experimental levers to modify the interface pattern (Part II). The different interface patterns obtained have concrete consequences for the optical properties of the synthesized HNCs with the modification of crucial photoluminescence characteristics such as the emission spectrum, and absolute upconversion quantum yield (UCQY) without changing the chemical composition of the core and shell sub-domains. The results presented in this article introduce a paradigm shift for improved synthesis concept(s) with better control over the atomic scale organization of Ln-based core-shell HNCs, which is of critical interest for the emergence of a new generation of such particles.

2. Results and Discussion

2.1. Core-Shell Hetero-Nanocrystals and Objectives

All synthesized core-shell HNCs rely on a single-shell architecture, which is formed by an optically active core (Yb^{3+}/Er^{3+} used as the sensitizer/activator pair in various proportions) combined to an optically inert shell ($NaYF_4$). An overview of all synthesized core NCs and core-shell HNCs is given in **Figure 2**. The investigated core-shell HNCs are split in two different sets (Figure 2, Set #1 and Set #2) to address various objectives.

Core-shell HNCs from Set #1 (Figure $2a_1$–c_1) were used to assess the capability of two independent characterization techniques to distinguish various types of interface pattern together with their corresponding spatial organization (Part I). Indeed, most literature dealing with interface patterns in core-shell Ln-based HNCs rely on optical measurements,[7a,d,13] which are not adapted to describe the spatial extension and magnitude of the alloying and/or cation exchange phenomena in core-shell

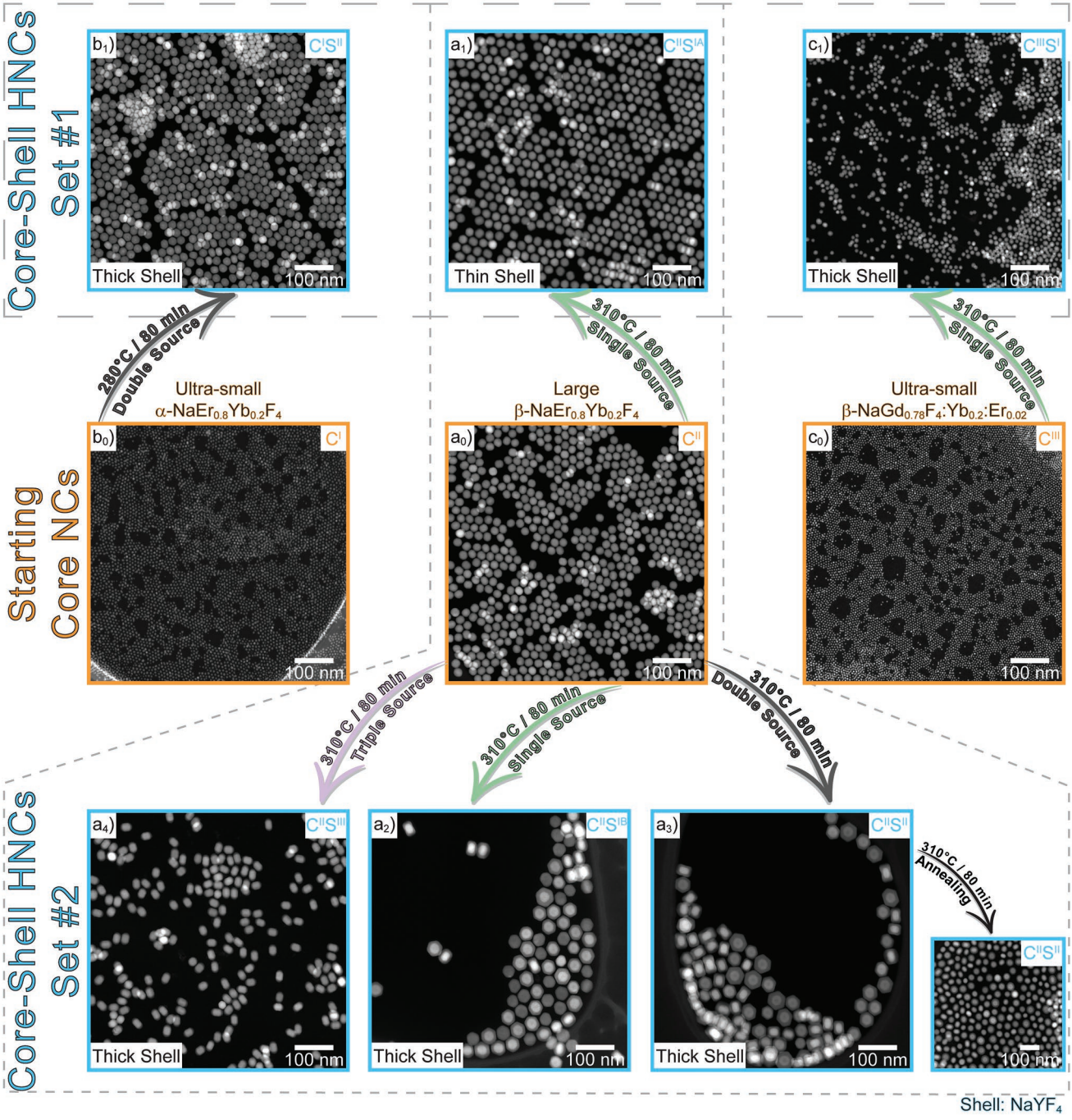

Figure 2. Low magnification high-angle annular dark-field scanning transmission electron microscopy (HAADF-STEM) images of (a_0-c_0) all core nanocrystals (NCs) and (a_1-c_1, a_2-a_4) core-shell hetero-nanocrystals (HNCs) synthesized. Curved arrows indicate which core NCs were used as the starting seeds for the growth of core-shell HNCs together with corresponding shell growth conditions. Single- (ultra-small α-NaYF4 sacrificial seeds), double-($Y(OOCCF_3)_3$ and $NaOOCCF_3$), and triple- ($Y(OOCCH_3)_3$, NaOH, NH_4F) source refer to the nature of shell precursor(s). All core-shell HNCs were synthesized by a controlled hot injection method in a mixture of oleic acid and octadecene. All NCs and HNCs are identified by a short code (top right corner of each HAADF-STEM image).

Ln-based HNCs. To overcome these limitations, microscopic methods must be employed and in particular scanning transmission electron microscopy (STEM)-based methods such as spatially resolved energy dispersive X-ray spectroscopy (EDXS). Moreover, to significantly improve resolution of spatially resolved EDXS/STEM analysis, the latter can be combined to the quantitative analysis of annular dark-field (ADF)-STEM images.[5a,14] Therefore, compared to optical spectroscopy, the previously mentioned STEM-based methods offer important improvements such as the characterization of single individual

particles (instead of an ensemble of particles) with a spatial resolution extending from about 1 nm down to the atomic-scale (depending on the method). This constitutes a considerable advantage to identify the correct interface pattern when synthesizing core-shell Ln-based HNCs under various synthetic conditions. Additionally, core-shell HNCs from Set #2 (Figure 2a_1–a_4) were used to identify how shelling conditions (shell precursors, relative shell thickness, post-synthesis annealing treatment) can be used to modify the type of interface pattern for a given single-shell architecture with fixed chemical composition both for the core ($NaEr_{0.8}Yb_{0.2}F_4$) and shell ($NaYF_4$) domains (Part II). Core-shell HNCs from both sets (#1 and #2) were used to investigate how the emission spectrum and absolute UCQY are influenced when modifying the interface pattern (Part III).

To improve reading efficiency but also to facilitate the identification of the different samples throughout the manuscript, all synthesized core-shell HNCs are identified by two capital letters (CS) together with attached superscript Roman numerals (Figure 2, top right corner of each HAADF-STEM images). The latter reflect i) the identity of core NCs that were used as starting seeds, and ii) the type of shell precursors injected for shell growth. Roman numerals affiliated to the core (C) refer to the use of either ultra-small cubic α-$NaEr_{0.8}Yb_{0.2}F_4$ (C^{I}, Figure 2b_0; Figure S1, Supporting Information), large hexagonal β-$NaEr_{0.8}Yb_{0.2}F_4$ (C^{II}, Figure 2a_0; Figure S1, Supporting Information), or ultra-small β-$NaGd_{0.78}F_4$:$Yb_{0.2}$:$Er_{0.02}$ (C^{III}, Figure 2c_0; Figure S2, Supporting Information) core NCs. Roman numerals affiliated to the shell (S) refer to the type of shell precursors injected for shell growth such as single source (S^{I}, ultra-small cubic α-$NaYF_4$ sacrificial seeds; Figure S3, Supporting Information), double source (S^{II}, $Y(OOCCF_3)_3$ and $NaOOCCF_3$), and triple source (S^{III}, $Y(OOCCH_3)_3$, NaOH, and NH_4F) precursors. All details regarding the synthesis of core NCs and core-shell HNCs are given in Sections S4,S5, Tables S1,S2, Supporting Information.

2.2. Part I: Identification and Characterization of Interface Patterns

Core-shell HNCs from Set #1 were first used to determine whether the reference characterization technique (i.e., spatially resolved EDXS/STEM analysis) previously used by the authors is able to distinguish between different types of interface pattern (in particular when a Type-I is formed). Additionally, to strengthen the validity of the conclusions but also to improve the resolution, spatially resolved EDXS/STEM analysis was coupled to a second independent characterization technique, which is based on a very different approach. Indeed, in the latter case, the chemical organization of a whole particle can be extracted from the quantitative analysis of its corresponding ADF-STEM image. At this point, it is important to note that core-shell HNCs from Set #1 ($C^{I}S^{II}$, $C^{II}S^{IA}$) were synthesized under different conditions (different core sizes, different shell thickness, etc.) because the primary objective was to obtain single-shell architectures with noticeably different interface patterns. Core-shell HNCs with thick ($C^{I}S^{II}$) and thin ($C^{II}S^{IA}$) shells were synthesized from ultra-small (5.9 ± 1.8 nm) cubic (C^{I}, Figure 2b_0; Table S1, Supporting Information) and large (23.8 ± 1.6 nm) hexagonal (C^{II}, Figure 2b_0; Table S1, Supporting Information) NCs. The obtained HNCs are fully crystalline (hexagonal structure in both case) and highly monodisperse isotropic particles with mean sizes of 20.4 ± 1.4 nm ($C^{I}S^{II}$; Figure S4,Table S2, Supporting Information) and 26.2 ± 1.8 nm ($C^{II}S^{IA}$; Figure S4, Table S2, Supporting Information). Compared to the size of the starting core particles, these values correspond to shell thicknesses (when considering the formation of a Type-I interface pattern) of ≈7 and 1 nm for HNCs with thick ($C^{I}S^{II}$) and thin ($C^{II}S^{IA}$) shell, respectively.

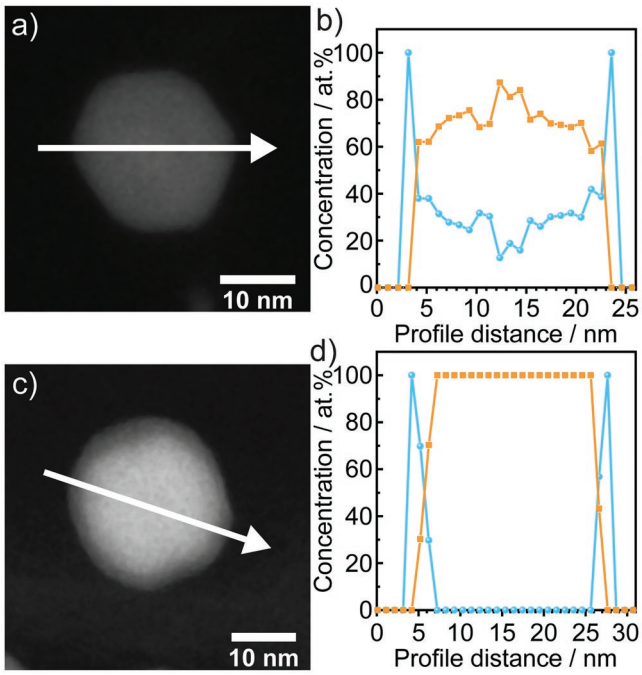

Figure 3. High-angle annular dark-field scanning transmission electron microscopy (HAADF-STEM) images (left column) and corresponding chemical concentration profiles (right column) of the particles shown in the left column. The concentration profiles were obtained from energy dispersive X-ray spectroscopy (EDXS)/STEM line profiles after implementing the subshell approach for thick-shell ($C^{I}S^{II}$, top row) and thin-shell ($C^{II}S^{IA}$, bottom row) hetero-nanocrystals synthesized from a,b) ultra-small α-$NaErF_4$:Yb and c,d) large β-$NaErF_4$:Yb core particles, respectively. White arrows indicate the EDXS scan direction. The erbium/ytterbium and yttrium concentration profiles are in orange and blue, respectively.

2.2.1. Spatially Resolved EDXS/STEM Analyses

The chemical composition of single $C^{I}S^{II}$ and $C^{II}S^{IA}$ HNCs was first characterized by spatially resolved EDXS/STEM analyses. For this purpose, the electron beam is focused to a small diameter (typically 0.5 nm) and EDX spectra are acquired successively with 1-nm step distance along a line through the center of single particles as indicated by the arrow in HAADF-STEM images (**Figure 3**, left column). Corresponding composition profiles (Figure 3, right column) were extracted from the quantified EDX spectra. At this point, it is important to emphasize that chemical profiles of shell (i.e., Y, blue line) and core (i.e.,

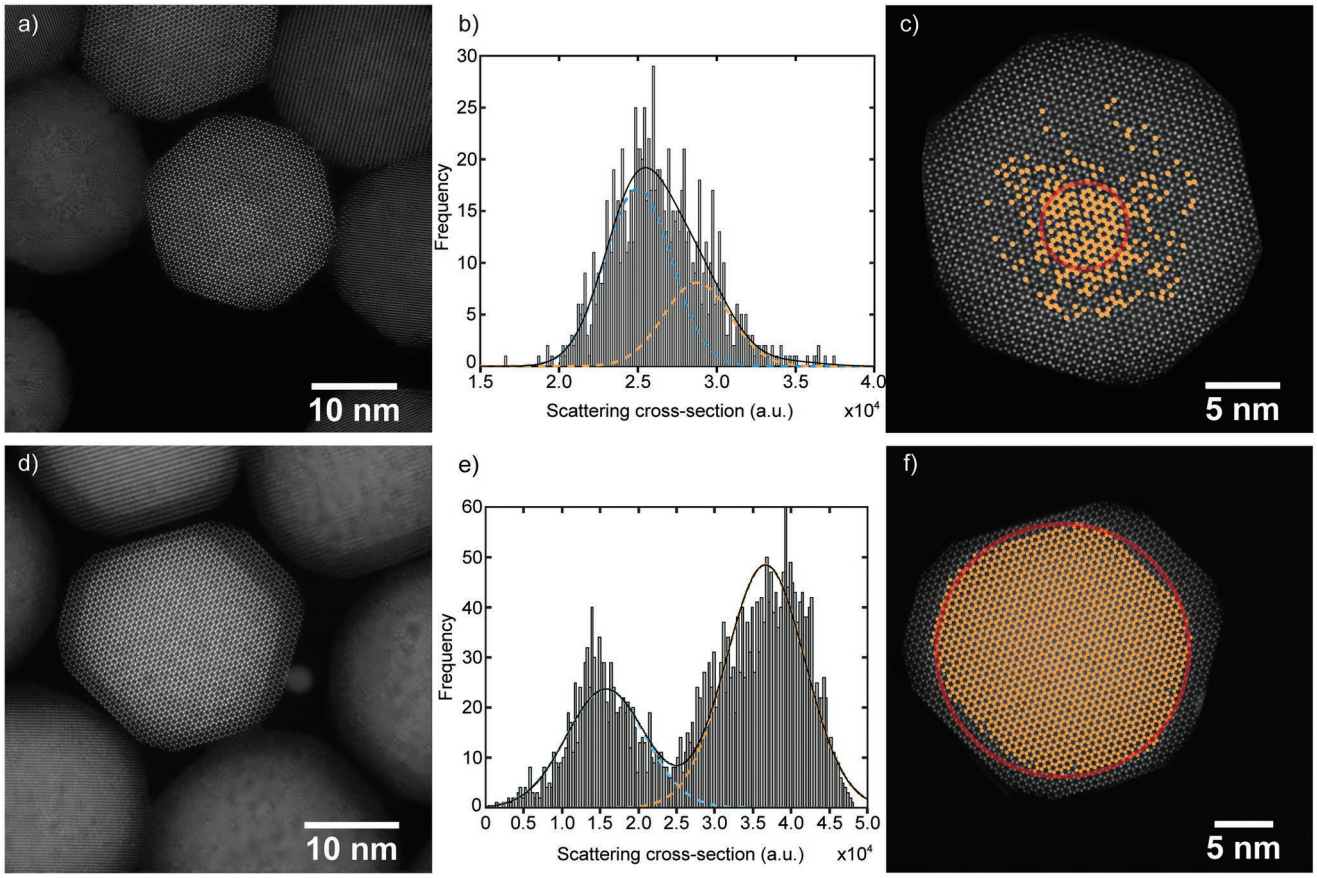

Figure 4. Corrected high-resolution annular dark-field scanning transmission electron microscopy (ADF-STEM) images after applying the convolutional neural network (left column), scattering cross section histograms together with the classification into two groups using a Gaussian mixture model with two components (middle column), and refined high-resolution ADF-STEM images (using the StatSTEM software) overlaid by maps (orange dots) reflecting the probability of finding at least one heavy lanthanide element (Er or Yb) for each atomic column within an individual β-$NaErF_4$:Yb@$NaYF_4$ HNC (right column). Data in the a–c) top and d–f) bottom rows correspond to C^IS^{II} and $C^{II}S^{IA}$ HNCs, respectively. Red circles in the refined high-resolution ADF-STEM images (c,f) indicate the initial size of the starting core particles (Figure S1, Supporting Information). Note that red circles are centered on the region with the highest density of atomic columns containing at least one heavy lanthanide element.

Yb/Er, orange line) elements shown in Figure 3 (right column) were obtained after processing the compositions (extracted from quantified EDX spectra) with the subshell approach outlined in detail by the authors in a review article.[5a] To summarize, raw compositions obtained from EDX spectra cannot be used to reveal the exact local chemical composition of core-shell HNCs without further processing because the electron beam propagates through the shell and core yielding an averaged chemical composition along the electron-beam direction. This limitation can be overcome by implementing the subshell approach where a single core-shell HNC is (mathematically) subdivided in concentric regions denoted as subshells (not to be confused with the real chemical shell) whose number is determined by the overall size of the particle and the distance (1 nm) between two successive EDXS acquisition points. As described in detail by the authors elsewhere,[5a] the subshell approach was used to process the raw compositions obtained from quantified EDX spectra. Such a data treatment eliminates the superposition of the shell and core contributions to the overall EDXS signal and yields the local chemical composition of each subshell and, hence, the real composition of the shell and core regions. Striking differences in the chemical profiles (Figure 3, right column) are immediately visible between C^IS^{II} and $C^{II}S^{IA}$ HNCs. Indeed, the alloying of Y and Yb/Er has occurred destroying entirely the chemical integrity of the starting core in the case of thick shell HNCs synthesized from ultra-small starting core particles (C^IS^{II}, Figure 3a,b), which corresponds to a Type-III interface pattern according to our definition (Figure 1).

On the contrary, a large and intact core domain is clearly visible in the case of thin shell HNCs synthesized from large starting core particles ($C^{II}S^{IA}$, Figure 3c,d). In this case, an abrupt transition between the pure core and pure shell domains with a width of about 1 nm is clearly visible, which corresponds to a Type-I interface pattern. These results demonstrate that spatially resolved EDXS/STEM analyses performed on C^IS^{II} and $C^{II}S^{IA}$ HNCs (Figure 3) can clearly distinguish between the formation of Type-III and Type-I interface patterns.

2.2.2. Quantitative Analysis of ADF-STEM Images

To validate the results obtained by spatially resolved EDXS/STEM analyses but also to improve the resolution, a

quantitative analysis of ADF-STEM images was performed on the same HNCs (C^IS^{II} and $C^{II}S^{IA}$). The method is based on the accurate quantification of the intensity of the different atomic columns in high-resolution ADF-STEM images obtained with a probe-corrected STEM (experimental details are given in the Section S6, Supporting Information). The acquired ADF-STEM images were corrected for distortions using a deep convolutional neural network (**Figure 4**, left column; Section S6, Supporting Information).[15] By using the StatSTEM software,[16] the projected atomic columns are modeled by a sum of Gaussian functions peaked at the atomic column positions. The volumes under these Gaussian peaks, the so-called scattering cross sections, scale with the chemical composition and thickness of a projected atomic column observed in the corresponding ADF-STEM image.[17]

The ADF-STEM image of an individual $C^{II}S^{IA}$ HNC (Figure 4d) synthesized from the large core particles with a thin shell deposition shows an abrupt transition between shell and core while the ADF-STEM image of an individual C^IS^{II} HNC (Figure 4a) synthesized from ultra-small core particles with a thick shell deposition does not show a sharp interface at the atomic scale. In order to unscramble the thickness and composition effects, the quantitative analysis was limited to the region where the thickness can be assumed to be constant. The distribution of scattering cross sections (histograms in Figure 4, middle column) is then used to classify the atomic columns into groups depending on their averaged chemical composition along the direction parallel to the incident beam. For this purpose, an analysis based on Gaussian mixture models is performed to fit the distribution of scattering cross sections with two components (blue and orange dashed lines in Figure 4, middle column). The first component (blue dashed line in Figure 4, middle column) contains scattering cross sections of the atomic columns resulting from the shell material (β-$NaYF_4$) without heavy lanthanides. On the contrary, the second component (orange dashed line in Figure 4, middle column) corresponds to scattering cross sections for the atomic columns that contain at least one heavy (Er or Yb) atom. Each scattering cross section can be assigned to the component having the highest probability for that particular scattering cross section. The atomic columns containing at least one heavy lanthanide element (i.e., Er or Yb) within an individual HNC and corresponding either to the thick- (C^IS^{II}) or thin- ($C^{II}S^{IA}$) shell are shown as orange dots overlaying the refined high-resolution ADF-STEM images in Figure 4c,f, respectively.

In the case of C^IS^{II} HNCs, which were synthesized from ultra-small C^I core particles, the comparison of the mean diameter before and after shell growth together with a Type-I interface model (assumed by default) indicate that the optically active elements should be confined in a sub-domain (i.e., the starting core) representing only 2% of the total volume of the final HNC and protected by a thick inert shell of 7.3 nm. In reality, the atomic-scale resolved map (Figure 4c) not only confirms the breakdown of the initially designed confinement but also the inhomogeneous redistribution of heavy lanthanide elements (supposed to be confined in the core domain) within a particle volume much larger than expected. Indeed, despite the impossibility to determine the relative positions (i.e., relative "heights") of heavy and light rare-earth elements within each atomic column, it seems legitimate to assume alloying in the electron-beam (z) direction with a magnitude similar to what is observed for the x- and y-directions. In this case, the particle volume (assuming a spherical approximation) where optically active heavy lanthanide elements (Er/Yb) can be found is 16-times larger than expected and represents 40% (instead of 2%) of the total volume of the HNC. Such a spatial redistribution is typical of a heterogeneous Type-III interface pattern. It is worth pointing out that atomic columns containing no heavy lanthanide elements can even be observed at the center of the HNC, clearly proving the total loss of the chemical integrity of the initial core domain. In the case of $C^{II}S^{IA}$, which were synthesized from large C^{II} core particles, the quantitative analysis of the corresponding ADF-STEM image indicates the formation of a Type-I interface (Figure 4f).

To be sure that the cubic (α) to hexagonal (β) phase transition undergone by the starting ultra-small C^I core particles during the shell deposition did not play a role in the formation of a Type-III interface pattern, a control experiment was performed with C^{III} core particles (Figure $2c_0$). Although the latter do not have the same chemical composition as C^I core particles (only large particles could be obtained with the hexagonal phase and the same chemical composition), their size is very similar (Table S1, Supporting Information). Results obtained by performing spatially resolved EDXS/STEM analyses on $C^{III}S^I$ HNCs also reveal the formation of a Type-III interface pattern (Figure S2, Supporting Information) ruling out the cubic to hexagonal phase transition as a driving force in the formation of a Type-III interface pattern. Similarly, the temperature difference in the growth of $C^{III}S^I$ HNCs compared to C^IS^{II} HNCs is not acting as the main driving force to trigger the formation of a Type-III interface pattern because such a behavior was also observed for HNCs synthesized at 290 °C as in the case of C^IS^{II} HNCs.[7b] Consequently, the ultra-small size of the starting core NCs is very likely the main origin leading to the formation of Type-III interface patterns.

The quantitative analysis of ADF-STEM images not only validates the results obtained by spatially resolved EDXS/STEM analysis but also enables a step forward in the accurate description of core-shell HNCs by revealing the distribution of core and shell elements for each atomic column within a single particle. It is important to emphasize that both methods lead to the same conclusions regarding the nature of the interface pattern when growing core-shell HNCs and can be used with confidence to reveal such essential structural features.

2.3. Part II: Modification of the Interface Pattern

In depth characterization of core-shell HNCs from Set #1 indicates that the size of the starting seeds can dramatically modify the type of interface pattern. The smaller the starting seeds, the higher the probability to lose the chemical integrity of the starting core domain. On the contrary, when large core particles are used as the starting seeds, an interface pattern with well defined core and shell domains is obtained together with an abrupt transition. Because core-shell HNCs from Set #1 were synthesized under different conditions (Figure 2, top panel; Table S2, Section S5, Supporting Information), the effect

of the latter on the type of interface pattern was investigated in a second stage. Therefore, using $C^{II}S^{IA}$ HNCs as a reference point (existence of a Type-I interface pattern), core-shell HNCs from Set #2 (Figure 2, bottom panel) were synthesized from the exact same starting core NCs (i.e., C^{II}, Figure 2a$_0$). Several parameters were modified (shell thickness, shell precursors, or post-synthesis annealing treatment) while the synthetic approach (controlled hot injection of shell precursors), chemical composition of the shell ($NaYF_4$), temperature (310 °C) and aging time (80 min) were kept constant (Section S5, Supporting Information).

2.3.1. Interface Pattern and Relative Shell Thickness

In a first step, the influence of the $NaYF_4$ shell thickness on the interface pattern was investigated by growing a thick shell ($C^{II}S^{II}$) instead of a thin one as in the case of $C^{II}S^{IA}$ HNCs. Under such conditions, large isotropic and highly faceted particles are formed together with anisotropic rod-like particles (**Figure 5**a; Figure S5, Supporting Information for the corresponding size distribution histograms). The corresponding spatially resolved EDXS/STEM analyses clearly indicate that the growth of a thicker $NaYF_4$ shell on large C^{II} core particles triggers a transition from a Type-I to a Type-II interface pattern for both isotropic (Figure 5b,c) and anisotropic (Figure 5d,e) particles. Indeed, in the case of isotropic particles, the thickness of the interphase increases by a factor 4 while the thickness of the pure $NaYF_4$ shell domain is multiplied by 5 compared to core-shell HNCs with a thin shell ($C^{II}S^{IA}$). A similar effect is observed for the anisotropic particles although the size of the pure core domain shrinks down to 13 nm (on average) compared to the 20 nm (on average) observed for the isotropic particles. This can be explained when inspecting the corresponding high-angle ADF (HAADF)-STEM images. While the shape of the pure core region is not modified in the case of isotropic particles (bright region in Figure 5b), it clearly appears that the core region is elongated (bright region in Figure 5d) in the case of anisotropic particles. These results clearly indicate that the size of the starting core NCs is not, on its own, a reliable parameter to predict a priori the type of interface pattern that will be formed after shell deposition.

2.3.2. Interface Pattern and Shell Precursors

In a second step, the role of the starting shell precursors (i.e., single-, double, or triple-source) in the transition from a Type-I to a Type-II interface pattern was investigated. When a single source shell precursor (i.e., ultra-small α-$NaYF_4$ sacrificial seeds) was used ($C^{II}S^{IB}$), the transition from a Type-I ($C^{II}S^{IA}$) to a Type-II interface pattern is observed (Figure S6, Supporting Information). Note that the corresponding chemical distribution profiles of the shell and core elements are similar to those obtained when using a double source shell precursor ($C^{II}S^{II}$, Figure 5). Moreover, a significant fraction of large isotropic particles of the pure shell material were formed together with isotropic and anisotropic core-shell HNCs (Figure S6, Supporting Information).

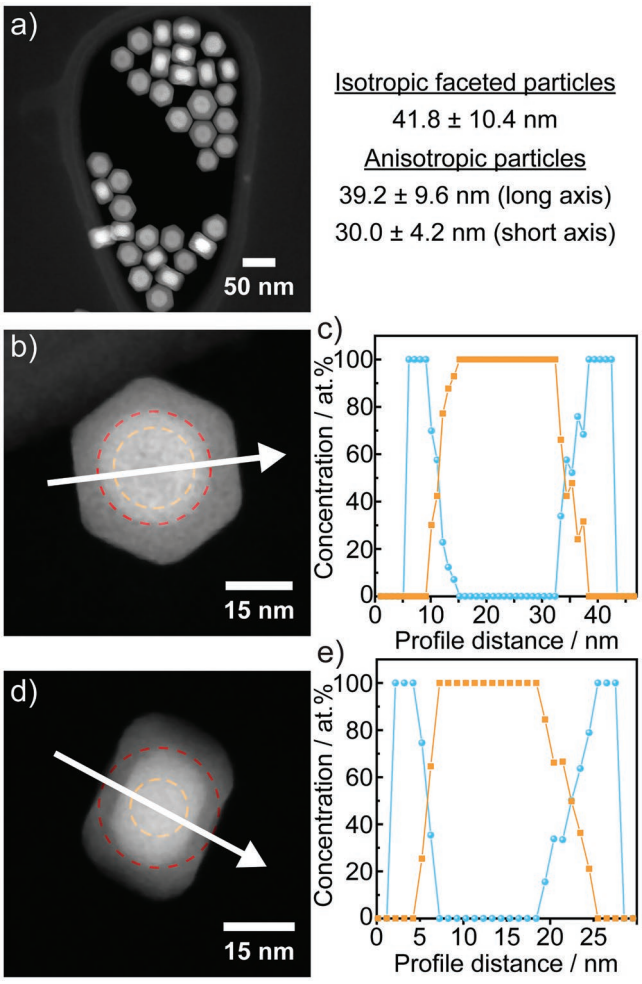

Figure 5. High-angle annular dark-field scanning transmission electron microscopy (HAADF-STEM) images (a,b,d) and chemical concentration profiles (c,e) of the particles shown in the left column. The concentration profiles were obtained from energy dispersive X-ray spectroscopy (EDXS)/STEM line profiles after implementing the subshell approach for thick-shell $C^{II}S^{II}$ hetero-nanocrystals (HNCs) synthesized from large β-$NaErF_4$:Yb core particles with yttrium and sodium trifluoroacetates as shell precursors for b,c) isotropic and d,e) anisotropic HNCs. The erbium/ytterbium and yttrium concentration profiles are in orange and blue, respectively. On HAADF-STEM images (b,d), white arrows indicate the EDXS scan direction while red and orange dashed circles indicate the initial size of the starting core particles together with the real size of the pure core domain (as determined by EDXS), respectively.

On the other hand, when a triple source shell precursor (i.e., yttrium acetate in combination with sodium hydroxide and ammonium fluoride) was used ($C^{II}S^{III}$), the shape of the synthesized core-shell HNCs was significantly different. Indeed, highly monodisperse anisotropic nanorods were obtained with average dimensions of 29.1 ± 3.0 and 21.0 ± 2.0 nm for the long and short axes, respectively (Figure S7, Supporting Information). Second, although the transition from a Type-I to a Type-II interface pattern is also observed as for single- and double source shell precursors, the width of the interface pattern is different along the short and long axes (Figure S7e, Supporting Information).

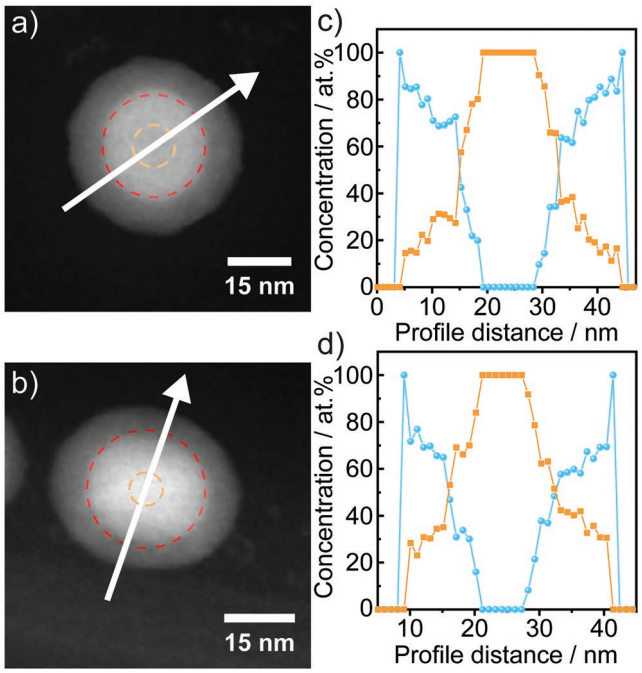

Figure 6. a,b) High-angle annular dark-field scanning transmission electron microscopy (HAADF-STEM) images (left column) and c,d) chemical concentration profiles (right column) of the particles shown in the left column. The composition profiles were obtained from energy dispersive X-ray spectroscopy EDXS/STEM line profiles after implementing the sub-shell approach for thick-shell $C^{II}S^{II}$ hetero-nanocrystals shown in Figure 4 but subsequently annealed at 310 °C for 80 min (without additional shell precursors). White arrows indicate the EDXS scan direction. The erbium/ytterbium and yttrium concentration profiles are in orange and blue, respectively. Red and orange dashed circles on HAADF images indicate the initial size of the starting core particles together with the real size of the pure core domain (as determined by EDXS), respectively.

2.3.3. Interface Pattern and Post-Synthesis Annealing

In a third step, the thermal stability of the interface pattern was investigated because of its importance when synthesizing multi-shell structures, which request multiple high temperature treatments. It is worth mentioning that the latter played a significant role in the development of the upconversion field over the past decade. $C^{II}S^{II}$ HNCs were selected to perform post-synthesis annealing treatment because such large particles should be less sensitive to thermal effects compared to smaller ones. After extraction and purification, the as-synthesized $C^{II}S^{II}$ HNCs (Figure 5) were annealed (in fresh solvent with the same composition as for their synthesis) at 310 °C for 80 min without injecting any additional shell precursors. The corresponding low magnification HAADF-STEM image (Figure S8, Supporting Information) indicates that the annealing treatment smooths the well-defined facets. This effect is observed for all HNCs, independently of their size or shape. More importantly, the spatially resolved EDXS/STEM analyses performed on the isotropic (**Figure 6**a,c) and anisotropic (Figure 6b,d) particles revealed that the interface pattern, although of Type-II as for the parent particles (Figure 5), is dramatically modified. Indeed, after annealing, the size of the pure core domain shrinks (on average) down to 10 nm for the isotropic particles, which is twice smaller compared to the size of the pure core domain that was identified directly after shell deposition and before annealing. At the same time, the average thickness of the interphase dramatically increases from 4 (before annealing) up to 13.5 nm (after annealing). Despite reverse concentration gradients, it is worth mentioning that optically active elements with a local concentration as high as 20 at% can be found at the outermost region of the interphase, which is very close to the surface. Therefore, the thickness of the protecting shell that only contains the optically inert element (Y) decreases down to 1.5 nm, which is ≈3.5 times thinner than before annealing. A similar trend is observed for the anisotropic particles (pure core domain: 7.5 nm, interface thickness: 11 nm with concentration gradients, pure inert shell thickness: 1 nm).

2.4. Part III: Interface Pattern and Photoluminescence Properties

One of the obvious differences between all synthesized HNCs is the modification of the color output under 980 nm excitation (**Figure 7**a,d). HNCs synthesized from the same optically active core particles (C^{II}) but with different shelling conditions are characterized by yellow (Figure 7a—$C^{II}S^{IA}$ HNCs), red (Figure 7b—$C^{II}S^{II}$ HNCs), and green-yellow (Figure 7c—$C^{II}S^{III}$ HNCs) colors under 980 nm excitation (300 W cm^{-2}). The inspection of the corresponding emission spectra indicates that both the red-to-green and red-to-near infrared (NIR) emission ratios are modified (Figure 7e–g) without changing the chemical composition of the core and shell domains. Taken with the above structural characterization, this is another evidence that the concentration of the active elements in the core-shell structures is affected by the shell growth conditions and alters the photoluminescence properties. Note that the effect of the concentration of optically active elements in the starting core particles on the output color is visible for HNCs synthesized from ultra-small β-$NaGdF_4$:Yb:Er with a dominant green emission over the red and NIR emissions (Figure 7d,h—$C^{III}S^{I}$ HNCs).

The mechanistic rationalization of the changes in emission spectra of such simple HNCs is challenging. Both the effective shell thickness (i.e., the shell thickness free from any optically active center) and interface pattern modulate relaxation channels (productive and deleterious). Nonetheless, that these parameters significantly affect the luminescence properties is clear; the latter are a consequence of the holistic core plus shell growth chemistries and processes.

The absolute UCQY, another photoluminescence property of major interest because of its significance for a wide range of potential applications, is also changed based on shell growth conditions. The UCQY was measured at different power densities for each HNCs (**Figure 8**—data points). It is clear that $C^{II}S^{IA}$ (Figure 8, curve ❶), $C^{II}S^{II}$ before (Figure 8, curve ❷) and after (Figure 8, curve ❹) annealing as well as $C^{II}S^{III}$ (Figure 8, curve ❸) have similar saturation effects. Therefore, the measured UCQY of these samples can be compared at 300 W cm^{-2} to get an impression of their relative performance. At 300 W cm^{-2}, measured values are 0.14% ($C^{II}S^{IA}$), 0.83% ($C^{II}S^{II}$ before annealing), 0.098% ($C^{II}S^{III}$), and 0.28% ($C^{II}S^{II}$ after annealing).

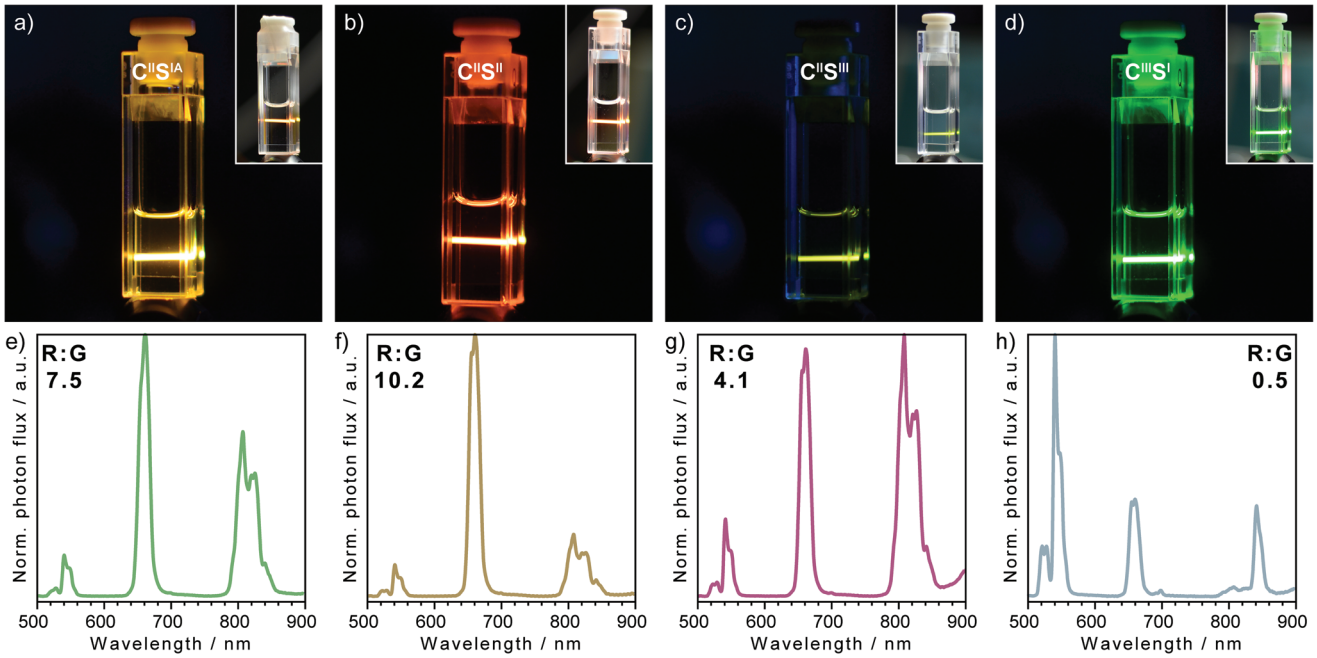

Figure 7. Photographs (top row) and emission spectra (bottom row) obtained under near-infrared excitation (980 nm at 300 W cm^{-2}) for various hetero-nanocrystals (HNCs) synthesized either from a–c,e–g) large β-$NaErF_4$:Yb or d,h) ultra-small β-$NaGdF_4$:Yb:Er core particles. HNCs from large β-$NaErF_4$:Yb core particles were synthesized under the same conditions (controlled hot-injection, 310 °C, 80 min) except for the shell thickness and/or shell precursors: (a,e) $C^{II}S^{IA}$ (thin shell, single source shell precursors), (b,f) $C^{II}S^{II}$ (thick shell, double source shell precursors), (c,g) $C^{II}S^{III}$ (thick shell, triple source shell precursors). (d,h) $C^{III}S^{I}$ HNCs synthesized by the controlled hot-injection method (310 °C, 80 min) from ultra-small β-$NaGdF_4$:Yb:Er core particles (C^{III}) and single source shell precursors (thick shell). All photographs were taken with the same digital camera (Nikon D700) equipped with an AF-Nikkor 50 mm 1:1.8D objective and with identical ISO (ISO 400), shutter speed (1/8 s), and aperture (f/2.2) settings.

Additionally, the critical power density (CPD) function that was described by Joseph and co-workers can be used as a supporting figure of merit to compare performances.[18] Indeed, the CPD function is useful to compare power densities for which the transition between the weak and strong excitation regimes happens. In the weak excitation regime, the number of generated UC photons is still non-linear dependent on the excitation photons number, with $N_{UC} \propto N_{exc.}^2$ in the case of a two-photon process. On the contrary, in the strong excitation regime, the system "saturates" and the probability of sequential energy transfer leading to UC is close to one with a typical linear dependence between the excitation and generated UC photons. In such a case, two 980 nm photons would be converted into one photon (one green or one red), four into two, three into six, etc. Therefore, in the strong excitation regime, the absolute UCQY does no longer depend on the power density. $\eta_{UC\text{-}Sat.}$ is estimated by fitting experimental power-dependent UCQY data with the CPD function (Figure 8—black solid lines). The CPD function not only can be used to determine the CPD but also to theoretically predict the maximum possible UCQY ($\eta_{UC\text{-}Sat.}$) that can be reached by a material. $C^{II}S^{IA}$ HNCs with a Type-I interface and an estimated $\eta_{UC\text{-}Sat.}$ of 0.23% together with a CPD value of 24 W cm^{-2} can be used as a reference for further evaluation (Figure 8, curve ❶, Type-I interface pattern). Interestingly, the growth of a thick inert shell on top of the same starting core particles (C^{II}) at the exact same temperature and aging time but using different shell precursors and shell growth methods can lead either to the strong increase (up to 1.1%) or decrease (down to 0.17%) of $\eta_{UC\text{-}Sat.}$ in the case of $C^{II}S^{II}$ (Figure 8, curve ❷, Type-II interface pattern) and $C^{II}S^{III}$ (Figure 8, curve ❸, Type-II interface pattern with unequal protection) HNCs, respectively. This can be explained by the structural features of the corresponding interface patterns. Whereas both types of HNCs are characterized by alloyed interface patterns, HNCs synthesized from yttrium and sodium trifluoroacetates ($C^{II}S^{II}$) clearly have a homogeneous protecting shell (i.e., free from optically active elements) while those synthesized from yttrium acetate in combination with sodium hydroxide and ammonium fluoride ($C^{II}S^{III}$) are not equally protected and in particular along the short axis. Such a structural feature favors energy migration toward surface quenching sites and explains the poorer UCQY and higher CPD value (30 W cm^{-2}). Interestingly, a post-synthesis annealing treatment of the most efficient (i.e., $C^{II}S^{II}$) HNCs (Figure 8, curve ❷) also leads to the deterioration of the saturation UCQY, which decreases from 1.1% down to 0.4% (Figure 8, curve ❹) while the CPD value increases from 6 up to 13 W cm^{-2}. Such a behavior is once again in agreement with the structural features of the interface pattern. Compared to their parent HNCs, the interface pattern after annealing is characterized by a much thicker alloyed region together with an effectively thinner protecting shell. Such a weaker degree of protection regarding surface quenching explains the weaker UCQY compared to the parent HNCs. Nonetheless, the UCQY is still double that compared to $C^{II}S^{IA}$ HNCs with a thin protecting shell and a Type-I interface pattern at all power densities (Figure 8, curve ❶). The influence of the thickness of the protecting shell can be ruled out because in both case the effective thickness is ≈1.5 nm. On the other hand, the thick alloyed

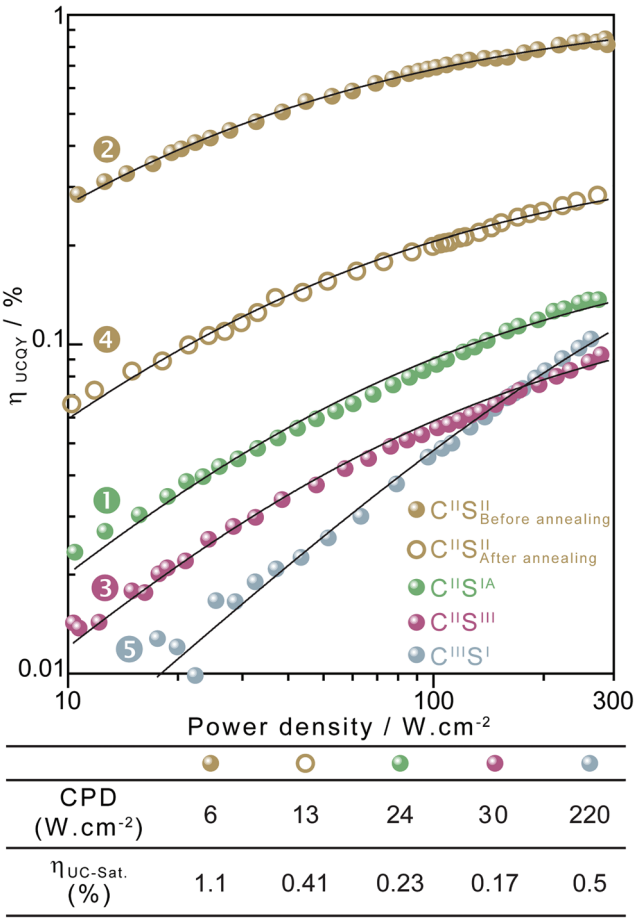

CPD ($W.cm^{-2}$)	6	13	24	30	220
$\eta_{UC\text{-}Sat.}$ (%)	1.1	0.41	0.23	0.17	0.5

Figure 8. Power-dependent ($\lambda_{ex.}$ = 980 nm) total absolute upconversion quantum yield (UCQY) for various hetero-nanocrystals (HNCs) synthesized from large β-$NaErF_4$:Yb (C^{II}) and ultra-small β-$NaGdF_4$:Yb:Er (C^{III}) core particles at 310 °C for 80 min (solid symbols) from single- (❶: $C^{II}S^{IA}$, ❺: $C^{III}S^{I}$), double- (❷: $C^{II}S^{II}$ before annealing,), and triple- (❸: $C^{II}S^{III}$) source shell precursors. Power-dependent UCQY of $C^{II}S^{II}$ HNCs after post-synthesis annealing treatment is also shown (❹). Fitting of the experimental data with a critical power density function (black solid lines) are shown together with the extracted critical power density (CPD) values and saturation upconversion quantum yield ($\eta_{UC\text{-}Sat.}$).

interface pattern of annealed HNCs led to the redistribution of the optically active centers in a much larger volume, thus decreasing their local concentration contrary to HNCs with a Type-I interface pattern, which is also proved by the larger CPD value (24 vs 13 W cm^{-2}). Consequently, the lower efficacy due to the thinner protecting shell (i.e., facilitated energy migration toward surface quenching sites) is counterbalanced by the dilution effect. If the latter would have been detrimental, the UCQY of annealed $C^{II}S^{II}$ HNCs (Figure 8, curve ❹) should be lower than that of $C^{II}S^{IA}$ HNCs with a Type-I interface pattern (Figure 8, curve ❶). This is not the case for any power density, thus indicating that concentration quenching is likely to remain a concern in Ln-based HNCs, as it is in bulk materials.

The importance of the dilution effect induced by the formation of an alloyed interface on the absolute UCQY is also noticeable in the case of $C^{III}S^{I}$ HNCs with a Type-III interface pattern (Figure 8, curve ❺). Contrary to the previously described HNCs, ultra-small β-$NaGdF_4$:Yb:Er core (C^{III}) particles with the "optimum" Yb^{3+} (18%) and Er^{3+} (2%) doping concentrations (i.e., derived from microcrystalline samples) were used for the growth of a thick protecting shell ($C^{III}S^{I}$). Although $C^{III}S^{I}$ HNCs have the worst UCQY at low power density, at the highest power density measured of 300 W cm^{-2}, it reaches the same UCQY value as for $C^{II}S^{IA}$ HNCs with a Type-I interface pattern (Figure 8, curves ❶,❺). It is worth noting that at much higher power density, the efficiency should even be higher than that of $C^{II}S^{II}$ HNCs after post-synthesis annealing treatment. Additionally, for the whole measurement range of power density, the slope of the power-dependent UCQY for $C^{III}S^{I}$ HNCs (Figure 8, curve ❺) remains constant and does not show any sign of saturation. The corresponding high CPD value (220 W cm^{-2}) together with the constant slope indicate that the energy transfer efficiency between optical centers is far from being optimized and requests much higher excitation photon flux to become efficient. In this case, increasing already optimized distances between optically active centers (due to the dilution effect) drastically reduced the rate of energy transfer between ions to sub-optimal levels. For comparison, within the same power density range, the saturating trend of UC generation efficiency (Figure 8, curves ❶–❹) and corresponding CPD values (6, 13, 24, and 30 W cm^{-2}) of all other heavily doped HNCs indicate that, even at low power density, energy-transfer UC is the dominant deactivation channel due to better energy transfer capabilities.

3. Discussion

Results obtained with core-shell HNCs from Set #1 clearly indicate that the size of the starting core NCs plays an important role regarding the type of interface pattern that is formed after shell growth. Additionally, results obtained with core-shell HNCs from Set #2 (same core with modified shell-growth conditions) revealed that the size of the starting core NCs is not, on its own, a reliable parameter to predict a priori the type of interface pattern that will be formed after shell growth. Indeed, the type of interface pattern obtained when synthesizing core-shell Ln-based HNCs results from complex interactions between various parameters (size of the starting seeds, relative shell thickness, shell precursors, and post-synthesis temperature annealing), which can influence mechanisms governing cation intermixing. Consequently, the results indicate that a one-size-fits-all model to describe the interface of core-shell Ln-based HNCs is a myth.

Because cation intermixing is a transport phenomenon involving atoms supposed to be confined in the core and shell domains, their net transport and intermixing happens at the atomic scale, which is a fundamental and critical issue. Although some important experimental parameters leading to different types of interface patterns were identified in this study,[19] the underlying mechanisms leading to cation intermixing are not clear. Cation intermixing can be due to several phenomena such as i) solid-state diffusion (interstitial and/or vacancy), ii) partial dissolution of the core followed by recrystallization in presence of shell precursors, and iii) a combination of the previous phenomena.

Although solid-state diffusion has been revealed as a complicated process in core-shell metal HNCs,[1a,4,20] such a mechanism has been considered to be negligible by several groups when considering core-shell Ln-based HNCs. For instance, Komban and co-workers showed that post-synthesis annealing of single-shell HNCs (β-$NaYF_4$-$NaGdF_4$, overall size ≈10 nm, 1 nm shell thickness) in pure oleylamine at 320 °C for 20 min does not trigger measurable solid-state diffusion.[21] This is in agreement with the data reported by Chen and co-workers who did not observe significant diffusion when annealing (350 °C for 120 min) solid-state powder of large single-shell HNCs (β-$NaYF_4$:Ce-$NaYF_4$:Tb, overall size ≈50 nm, 3 nm shell thickness).[13a] Nevertheless, Liu and co-workers recently noticed discrepancies and reported diffusion[22] in large single-shell HNCs (β-$NaErF_4$-$NaREF_4$ with RE = Y, Gd, or Lu, overall size ≈23, 30, or 40 nm, 1-, 5-, or 10 nm shell thickness) after annealing the as-synthesized HNCs in the same mother mixture (oleic acid and octadecene) as used for their growth.[13b] Liu and co-workers reported diffusion for annealing treatments in the temperature range 200–300 °C with increased magnitude above 280 °C. Note that in the study reported by Liu and co-workers, single-shell HNCs were submitted to very long annealing time ranging from 120 up to 720 min.

Interestingly, investigations for which no trace of cation intermixing was reported relied on experiments either performed in the solid-state (Chen et al.[13a]) or in the liquid state but in the absence of oleic acid (Komban et al.[21]). This particular point is important because the vast majority of synthetic approaches used for the liquid-state synthesis of single- and multi-shell $NaLnF_4$-based HNCs rely on the use of oleic acid (in combination with octadecene and/or oleylamine). Oleic acid is recognized to promote the dissolution of crystalline (cubic or hexagonal) $NaLnF_4$ particles, thus releasing soluble species when heated in a fresh mixture of oleic acid and octadecene.[23] Such a dissolution process continues until an equilibrium is reached. Thus, it is clear that in the presence of shell precursors in solution, both core and shell elements can recrystallize through the formation of an alloy. This can easily happen because $NaLnF_4$ compounds constitute a class of isostructural phases with limited lattice mismatch (<5%) and significant miscibility over a wide range of Ln composition (including rare earth elements).

Because dissolution kinetics are much faster for smaller particles compared to larger ones, this can explain why a Type-III interface pattern was only observed for core-shell HNCs synthesized from ultra-small starting seeds (C^IS^{II} and $C^{III}S^I$). The dissolution and recrystallization mechanism together with the redistribution of cations from the core and shell domains (transition from a Type-I to a Type-II interface pattern) could also explain why sharp edges observed after the synthesis of large core-shell HNCs ($C^{II}S^{II}$) disappeared after temperature annealing in fresh oleic acid/octadecene. Note that particle resphering is not unusual and was observed by Wu and co-workers for Pd-Au HNCs at 400 °C during solid-state annealing.[24] Although the dissolution and recrystallization mechanism is very likely to happen, it cannot explain on its own why a transition from a Type-I to a Type-II interface pattern was observed for $C^{II}S^{IA}$ and $C^{II}S^{IB}$ HNCs, respectively. This suggests that solid-state diffusion exists but might be controlled by the concentration difference of core and shell elements in the particles and in solution. It is also important to emphasize that a liquid coordinating environment can dramatically influence the diffusion process during shell growth and/or post-synthesis annealing treatment. Indeed, the redissolution of $NaLnF_4$ NCs significantly disturbs their corresponding surface with increased surface and/or subsurface defect concentration, which can be trapped during the recrystallization process. If the case, the newly created defects (e.g., vacancies) can act as a powerful driving force to modify solid-state diffusion rates. Consequently, one can legitimately assume that a convolution of mechanisms is responsible for cation intermixing during the synthesis of core-shell Ln-based HNCs.

The spatially resolved EDXS/STEM analyses and the quantification of ADF-STEM images performed on large HNCs indicate that their internal structure and not just the region close to the surface can be deeply modified. Such an uncontrolled internal redistribution can lead to significant modifications of the emission and absolute UCQY of the exact same type of architecture (single shell β-$NaErF_4$:Yb-$NaYF_4$ architecture) without changing the chemical composition of the core and shell domains. The chemical identity (i.e., nature and concentration of optically active and inert elements) of the different domains that constitute HNCs must take into account the magnitude of intermixing. By modulating (more or less significantly) the spatial distribution of the optically active centers, the interface pattern is responsible for the alteration of both the nearest neighbor distances, local concentrations, and pathways to the HNC surface. To optimize the absolute UCQY, optimized concentrations must be determined for a given architecture (single- or multi-shell) with a perfectly characterized interface pattern. The highest absolute UCQY value measured for $C^{II}S^{II}$ before annealing (0.6% at 100 W cm^{-2}, $\eta_{UC\text{-}SAT}$ = 1.1%) is comparable to the typical values reported in the literature and ranging from 0.2% up to 1% at 100 W cm^{-2} or lower (single-shell HNCs).[7b,11f,25] Nevertheless, it is worth mentioning that a comparison between absolute UCQY values reported in the literature is challenging because different i) host matrices, ii) chemical composition of optically active elements, and iii) synthetic methods can be used for the synthesis of core-shell HNCs. It is also important to emphasize that core-shell HNCs reported in this study were not designed to maximize the absolute UCQY but to investigate the effect of various parameters on the modification of the interface pattern and the consequences for the photoluminescence properties. When optimizing the design, Hudry et al. reported one of the best absolute UCQY values (3.5% at 60 W cm^{-2} for 19 nm triple-shell HNCs),[26] which is very close from the value reported by Homann and co-workers with an absolute UCQY value of 5% at 30 W cm^{-2} for 22 nm single-shell HNCs.[27] To the best of our knowledge, the same authors reported the record absolute UCQY value (9% at 30 W cm^{-2}) for 45 nm single-shell HNCs. Interestingly, Homann and co-workers synthesized their single-shell HNCs under drastically anhydrous conditions by removing all sources of hydroxide groups (HO^-), which can substitute fluoride anions in the crystal structure, and thus, act as luminescence quenching centers. One can anticipate that combining strictly anhydrous conditions for the synthesis of core-shell HNCs together with proper considerations regarding the interface pattern might be the key to design ultra-small but

very bright upconversion HNCs at low power excitation densities (<1 W cm^{-2}),[25a] which is of critical interest for in vivo biomedical applications.

4. Conclusions and Outlook

In this article, it was demonstrated that the outcome of the synthesis of core-shell Ln-based HNCs can easily and significantly deviate from the initially anticipated structure with abrupt interface. Such deviations were identified and characterized by STEM-based methods (ADF-STEM images and spatially resolved EDXS/STEM), which gave coherent indications regarding the type of interface pattern. The latter, which reflects the chemical and structural organization of the boundary/discontinuity region between two sub-domains (core-shell in this article), appears to be an important and useful notion to properly describe the atomic-scale organization of core-shell Ln-based HNCs. The experimental results showed that the interface pattern can be engineered from abrupt to diffuse, with the possibility to modulate the magnitude of the latter. Although the size of the starting core particles is important, it was demonstrated that such a parameter is not reliable, on its own, to predict which type of interface pattern will be formed. Indeed, interface patterns ranging from segregated (Type-I) to partial alloying (Type-II) were identified in $NaErF_4$:Yb-$NaYF_4$ HNCs grown from the same large starting core particles. Finally, without changing the overall architecture (i.e., single-shell only) or the chemical nature of the core and shell materials, important photoluminescence properties such as the emission spectrum and absolute UCQY of HNCs synthesized with various shelling conditions were modified.

Accurate models coupled to the comprehensive understanding of intermixing mechanisms will significantly improve the ability to control the atomic scale organization of Ln-based HNCs. This constitutes a difficult task and it is important to emphasize that the investigations performed in this article just scratched the surface of an entire field of research that was largely unexplored since the emergence of core-shell Ln-based HNCs nearly two decades ago. Consequently, a concerted effort within the upconversion scientific community is urgently needed to identify the conditions under which a specific type of interface pattern can be stabilized. Such interface pattern stability diagrams should also take into account the role of the initial lattice mismatch, chemical miscibility between the sub-domains involved in the designed structure, or the quantity of hydroxide groups.[27,28] Interface pattern stability diagrams for core-shell Ln-based HNCs might be used as a fundamental pillar not only for the comprehensive understanding of the structure-property relationships and the rational design (i.e., adapted to a specific application with a particular set of requirements in terms of optical characteristics), but also for the controlled synthesis of a new generation of core-shell Ln-based HNCs with improved or even new properties. Such a fundamental aspect is perfectly in line with some of the challenges the upconversion scientific community is currently facing to either explain optical behavior[9b,c] or improve important characteristics for technological applications.[29] This new field of research is of critical interest to prevent uncontrolled structural/chemical randomness and deviations from the initially designed structures, which might seriously compromise the successful translation of core-shell Ln-based HNCs from bench to market.

Supporting Information

Supporting Information is available from the Wiley Online Library or from the author.

Acknowledgements

The authors would like to acknowledge the financial support provided by the Helmholtz Recruitment Initiative Fellowship (B.S.R.) and the Helmholtz Association's Research Field Energy (Materials and Technologies for the Energy Transition program, Topic 1 Photovoltaics and Wind Energy). The authors would like to thank the Karlsruhe Nano Micro Facility (KNMF) for STEM access. This project has received funding from the European Research Council (ERC) under the European Union's Horizon 2020 Research and Innovation Programme (Grant agreement no. 770887 PICOMETRICS to S.V.A. and Grant agreement no. 815128 REALNANO to S.B.). The authors acknowledge financial support from the Research Foundation Flanders (FWO, Belgium) through Projects no. G.0502.18N, G.0267.18N, and a postdoctoral grant to A.D.B. T.A. acknowledges funding from the University of Antwerp Research fund (BOF). This project had received funding (EUSMI proposal #E181100205) from the European Union's Horizon 2020 Research and Innovation Programme under Grant agreement no 731019 (EUSMI). D.H. would like to thank "CGFigures" for helpful tutorials on 3D graphics with Blender.

Open access funding enabled and organized by Projekt DEAL.

Conflict of Interest

The authors declare no conflict of interest.

Data Availability Statement

The data that support the findings of this study are available on request from the corresponding author. The data are not publicly available due to privacy or ethical restrictions.

Keywords

core-shell, electron microscopy, interface, nanocrystals, upconversion

Received: July 27, 2021
Revised: September 1, 2021
Published online:

[1] a) D. Wu, K. Kusada, H. Kitagawa, *Sci. Technol. Adv. Mater.* **2016**, *17*, 583; b) L. De Trizio, L. Manna, *Chem. Rev.* **2016**, *116*, 10852; c) R. E. Schaak, B. C. Steimle, J. L. Fenton, *Acc. Chem. Res.* **2020**, *53*, 2558.

[2] a) A. Nelson, S. Honrao, R. G. Hennig, R. D. Robinson, *Chem. Mater.* **2019**, *31*, 991; b) A. C. Berends, W. van der Stam, J. P. Hofmann, E. Bladt, J. D. Meeldijk, S. Bals, C. de Mello Donega, *Chem. Mater.* **2018**, *30*, 2400; c) J. Liu, J. Zhang, *Chem. Rev.* **2020**, *120*, 2123.

[3] a) E. Hofman, A. Khammang, J. T. Wright, Z.-J. Li, P. F. McLaughlin, A. H. Davis, J. M. Franck, A. Chakraborty, R. W. Meulenberg, W. Zheng, *J. Phys. Chem. Lett.* **2020**, *11*, 5992; b) K. P. Acharya, H. M. Nguyen, M. Paulite, A. Piryatinski, J. Zhang, J. L. Casson, H. Xu, H. Htoon, J. A. Hollingsworth, *J. Am. Chem. Soc.* **2015**, *137*, 3755; c) F. García-Santamaría, S. Brovelli, R. Viswanatha, J. A. Hollingsworth, H. Htoon, S. A. Crooker, V. I. Klimov, *Nano Lett.* **2011**, *11*, 687; d) A. Rubin-Brusilovski, Y. Jang, A. Shapiro, A. Safran, A. Sashchiuk, E. Lifshitz, *Chem. Mater.* **2016**, *28*, 9056; e) V. Pinchetti, F. Meinardi, A. Camellini, G. Sirigu, S. Christodoulou, W. K. Bae, F. De Donato, L. Manna, M. Zavelani-Rossi, I. Moreels, V. I. Klimov, S. Brovelli, *ACS Nano* **2016**, *10*, 6877; f) E. Hofman, R. J. Robinson, Z.-J. Li, B. Dzikovski, W. Zheng, *J. Am. Chem. Soc.* **2017**, *139*, 8878; g) G. Gariano, V. Lesnyak, R. Brescia, G. Bertoni, Z. Dang, R. Gaspari, L. De Trizio, L. Manna, *J. Am. Chem. Soc.* **2017**, *139*, 9583.

[4] a) M. Schnedlitz, D. Knez, M. Lasserus, F. Hofer, R. Fernández-Perea, A. W. Hauser, M. P. Lara-Castells, W. E. Ernst, *J. Phys. Chem. C* **2020**, *124*, 16680; b) S. Bogatyrenko, A. Kryshtal, A. Kruk, O. Skryl, *J. Phys. Chem. C* **2020**, *124*, 25805; c) C. Yang, B. H. Ko, S. Hwang, Z. Liu, Y. Yao, W. Luc, M. Cui, A. S. Malkani, T. Li, X. Wang, J. Dai, B. Xu, G. Wang, D. Su, F. Jiao, L. Hu, *Sci. Adv.* **2020**, *6*, eaaz6844; d) T. Ishimoto, M. Koyama, *J. Phys. Chem. Lett.* **2016**, *7*, 736.

[5] a) D. Hudry, I. A. Howard, R. Popescu, D. Gerthsen, B. S. Richards, *Adv. Mater.* **2019**, *31*, 1900623; b) N. J. Johnson, F. J. M. Veggel, *Nano Res.* **2013**, *6*, 547; c) Y. Fan, L. Liu, F. Zhang, *Nano Today* **2019**, *25*, 68.

[6] a) H. Dong, L.-D. Sun, C.-H. Yan, *Nanoscale* **2013**, *5*, 5703; b) H.-S. Qian, Y. Zhang, *Langmuir* **2008**, *24*, 12123; c) F. Vetrone, R. Naccache, V. Mahalingam, C. G. Morgan, J. A. Capobianco, *Adv. Funct. Mater.* **2009**, *19*, 2924; d) F. Wang, R. Deng, J. Wang, Q. Wang, Y. Han, H. Zhu, X. Chen, X. Liu, *Nat. Mater.* **2011**, *10*, 968.

[7] a) S. Dühnen, M. Haase, *Chem. Mater.* **2015**, *27*, 8375; b) D. Hudry, D. Busko, R. Popescu, D. Gerthsen, A. M. M. Abeykoon, C. Kübel, T. Bergfeldt, B. S. Richards, *Chem. Mater.* **2017**, *29*, 9238; c) D. Hudry, R. Popescu, D. Busko, M. Diaz-Lopez, M. Abeykoon, P. Bordet, D. Gerthsen, I. A. Howard, B. S. Richards, *J. Mater. Chem. C* **2019**, *7*, 1164; d) P. U. Bastian, S. Nacak, V. Roddatis, M. U. Kumke, *J. Phys. Chem. C* **2020**, *124*, 11229.

[8] a) F. C. J. M. van Veggel, C. Dong, N. J. J. Johnson, J. Pichaandi, *Nanoscale* **2012**, *4*, 7309; b) K. A. Abel, J.-C. Boyer, C. M. Andrei, F. C. J. M. van Veggel, *J. Phys. Chem. Lett.* **2011**, *2*, 185; c) C. Dong, F. C. J. M. van Veggel, *ACS Nano* **2009**, *3*, 123.

[9] a) Y. Zhang, X. Zhu, Y. Zhang, *ACS Nano* **2021**, *15*, 3709; b) G. Tessitore, G. A. Mandl, M. G. Brik, W. Park, J. A. Capobianco, *Nanoscale* **2019**, *11*, 12015; c) R. Shi, E. D. Martinez, C. D. S. Brites, L. D. Carlos, *Phys. Chem. Chem. Phys.* **2021**, *23*, 20; d) X. Zhu, J. Zhang, J. Liu, Y. Zhang, *Adv. Sci.* **2019**, *6*, 1901358.

[10] F. Auzel, *Chem. Rev.* **2004**, *104*, 139.

[11] a) A. Nadort, J. Zhao, E. M. Goldys, *Nanoscale* **2016**, *8*, 13099; b) L. Tu, X. Liu, F. Wu, H. Zhang, *Chem. Soc. Rev.* **2015**, *44*, 1331; c) E. M. Chan, E. S. Levy, B. E. Cohen, *Adv. Mater.* **2015**, *27*, 5753; d) Q. Su, S. Han, X. Xie, H. Zhu, H. Chen, C.-K. Chen, R.-S. Liu, X. Chen, F. Wang, X. Liu, *J. Am. Chem. Soc.* **2012**, *134*, 20849; e) H. Wen, H. Zhu, X. Chen, T. F. Hung, B. Wang, G. Zhu, S. F. Yu, F. Wang, *Angew. Chem., Int. Ed.* **2013**, *52*, 13419; f) X. Li, D. Shen, J. Yang, C. Yao, R. Che, F. Zhang, D. Zhao, *Chem. Mater.* **2013**, *25*, 106; g) J. Wang, R. Deng, M. A. MacDonald, B. Chen, J. Yuan, F. Wang, D. Chi, T. S. Andy Hor, P. Zhang, G. Liu, Y. Han, X. Liu, *Nat. Mater.* **2014**, *13*, 157; h) X. Li, R. Wang, F. Zhang, D. Zhao, *Nano Lett.* **2014**, *14*, 3634; i) M. Quintanilla, F. Ren, D. Ma, F. Vetrone, *ACS Photonics* **2014**, *1*, 662; j) R. Deng, F. Qin, R. Chen, W. Huang, M. Hong, X. Liu, *Nat. Nanotechnol.* **2015**, *10*, 237; k) X. Zhang, W. Chen, X. Xie, Y. Li, D. Chen, Z. Chao, C. Liu, H. Ma, Y. Liu, H. Ju, *Angew. Chem., Int. Ed.* **2019**, *58*, 12117; l) M. Wu, L. Yan, T. Wang, B. Zhou, Q. Zhang, *Adv. Funct. Mater.* **2019**, *29*, 1804160.

[12] a) H.-X. Mai, Y.-W. Zhang, L.-D. Sun, C.-H. Yan, *J. Phys. Chem. C* **2007**, *111*, 13721; b) G.-S. Yi, G.-M. Chow, *Chem. Mater.* **2007**, *19*, 341; c) J.-C. Boyer, J. Gagnon, L. A. Cuccia, J. A. Capobianco, *Chem. Mater.* **2007**, *19*, 3358; d) H. Schäfer, P. Ptacek, O. Zerzouf, M. Haase, *Adv. Funct. Mater.* **2008**, *18*, 2913.

[13] a) B. Chen, D. Peng, X. Chen, X. Qiao, X. Fan, F. Wang, *Angew. Chem., Int. Ed.* **2015**, *54*, 12788; b) L. Liu, X. Li, Y. Fan, C. Wang, A. M. El-Toni, M. S. Alhoshan, D. Zhao, F. Zhang, *Chem. Mater.* **2019**, *31*, 5608.

[14] a) C. Kind, R. Popescu, R. Schneider, E. Muller, D. Gerthsen, C. Feldmann, *RSC Adv.* **2012**, *2*, 9473; b) K. H. W. van den Bos, T. Altantzis, A. De Backer, S. Van Aert, S. Bals, *Adv. Phys.: X* **2018**, *3*, 1480420; c) S. Van Aert, A. De Backer, G. T. Martinez, A. J. den Dekker, D. Van Dyck, S. Bals, G. Van Tendeloo, *IUCrJ* **2016**, *3*, 71.

[15] T. Altantzis, I. Lobato, A. De Backer, A. Béché, Y. Zhang, S. Basak, M. Porcu, Q. Xu, A. Sánchez-Iglesias, L. M. Liz-Marzán, G. Van Tendeloo, S. Van Aert, S. Bals, *Nano Lett.* **2019**, *19*, 477.

[16] A. De Backer, K. H. W. van den Bos, W. Van den Broek, J. Sijbers, S. Van Aert, *Ultramicroscopy* **2016**, *171*, 104.

[17] S. Van Aert, J. Verbeeck, R. Erni, S. Bals, M. Luysberg, D. V. Dyck, G. V. Tendeloo, *Ultramicroscopy* **2009**, *109*, 1236.

[18] R. E. Joseph, C. Jiménez, D. Hudry, G. Gao, D. Busko, D. Biner, A. Turshatov, K. Krämer, B. S. Richards, I. A. Howard, *J. Phys. Chem. A* **2019**, *123*, 6799.

[19] The existence of additional unidentified parameters having an influence on the interface pattern is very likely.

[20] a) M. Schnedlitz, R. Fernandez-Perea, D. Knez, M. Lasserus, A. Schiffmann, F. Hofer, A. W. Hauser, M. P. de Lara-Castells, W. E. Ernst, *J. Phys. Chem. C* **2019**, *123*, 20037; b) B. Huang, H. Kobayashi, T. Yamamoto, S. Matsumura, Y. Nishida, K. Sato, K. Nagaoka, S. Kawaguchi, Y. Kubota, H. Kitagawa, *J. Am. Chem. Soc.* **2017**, *139*, 4643; c) G. Xiong, J. N. Clark, C. Nicklin, J. Rawle, I. K. Robinson, *Sci. Rep.* **2014**, *4*, 6765.

[21] R. Komban, J. P. Klare, B. Voss, J. Nordmann, H.-J. Steinhoff, M. Haase, *Angew. Chem., Int. Ed.* **2012**, *51*, 6506.

[22] The authors did not use the term "elemental migration" but refer to a vacancy assisted mechanism, which is typical of solid-state diffusion.

[23] B. Voss, M. Haase, *ACS Nano* **2013**, *7*, 11242.

[24] Z. Wu, M. Tang, X. Li, S. Luo, W. Yuan, B. Zhu, H. Zhang, H. Yang, Y. Gao, Y. Wang, *Phys. Chem. Chem. Phys.* **2019**, *21*, 3134.

[25] a) S. L. Maurizio, G. Tessitore, K. W. Krämer, J. A. Capobianco, *ACS Appl. Nano Mater.* **2021**, *4*, 5301; b) S. Fischer, R. D. Mehlenbacher, A. Lay, C. Siefe, A. P. Alivisatos, J. A. Dionne, *Nano Lett.* **2019**, *19*, 3878; c) D. J. Gargas, E. M. Chan, A. D. Ostrowski, S. Aloni, M. V. P. Altoe, E. S. Barnard, B. Sanii, J. J. Urban, D. J. Milliron, B. E. Cohen, P. J. Schuck, *Nat. Nanotechnol.* **2014**, *9*, 300.

[26] D. Hudry, D. Busko, R. Popescu, D. Gerthsen, I. A. Howard, B. S. Richards, *J. Mater. Chem. C* **2019**, *7*, 7371.

[27] C. Homann, L. Krukewitt, F. Frenzel, B. Grauel, C. Würth, U. Resch-Genger, M. Haase, *Angew. Chem., Int. Ed.* **2018**, *57*, 8765.

[28] a) J. Zhao, B. Chen, F. Wang, *Adv. Mater.* **2020**, *32*, 2004142; b) H. Ning, L. Jing, Y. Hou, S. Kalytchuk, Y. Li, X. Huang, M. Gao, *ACS Appl. Mater. Interfaces* **2020**, *12*, 11934; c) H. Dong, L.-D. Sun, L.-D. Li, R. Si, R. Liu, C.-H. Yan, *J. Am. Chem. Soc.* **2017**, *139*, 18492; d) L. Wang, L. Ren, D. Mitchell, G. Casillas-Garcia, W. Ren, C. Ma, X. X. Xu, S. Wen, F. Wang, J. Zhou, X. Xu, W. Hao, S. X. Dou, Y. Du, *Nanoscale* **2017**, *9*, 18661; e) N. J. J. Johnson, F. C. J. M. van Veggel, *ACS Nano* **2014**, *8*, 10517.

[29] a) J. R. Casar, C. A. McLellan, C. Siefe, J. A. Dionne, *ACS Photonics* **2021**, *8*, 3; b) H. Oliveira, A. Bednarkiewicz, A. Falk, E. Fröhlich, D. Lisjak, A. Prina-Mello, S. Resch, C. Schimpel, I. V. Vrček, E. Wysokińska, H. H. Gorris, *Adv. Healthcare Mater.* **2019**, *8*, 1801233.